Solid Freeform Fabrication 2023: Proceedings of the 34th Annual International Solid Freeform Fabrication Symposium – An Additive Manufacturing Conference
Reviewed Paper

UNIAXIAL FATIGUE BEHAVIOR AND LIFE PREDICTION OF ADDITIVELY MANUFACTURED INCONEL 718 WITH DIFFERENT GRAIN MORPHOLOGY

Muztahid Muhammad[1,2], Sajith Soman[1,2], Nabeel Ahmad[1,2], Douglas N. Wells[3], Shuai Shao[1,2], Nima Shamsaei[1,2*]

[1] National Center for Additive Manufacturing Excellence (NCAME), Auburn University, Auburn, AL 36849, USA

[2] Department of Mechanical Engineering, Auburn University, Auburn, AL 36849, USA
[3]NASA Marshall Space Flight Center, Huntsville, AL, 35812, USA

[*]Corresponding author: shamsaei@auburn.edu
Phone: (334) 844-4839

Abstract

Understanding the fatigue behavior and failure mechanisms is essential for qualifying and standardizing additively manufactured metallic components. This study investigates the uniaxial fatigue behavior and failure mechanisms of laser powder bed fused (L-PBF) Inconel 718 (IN718) specimens with different grain sizes obtained by altering the process parameters and heat treatment. Uniaxial, fully-reversed strain-controlled fatigue tests were conducted on specimens with machined and polished surface conditions. Microstructural analysis and fractography using a scanning electron microscope were performed to measure the sizes of grains and facets. Fatigue cracks were initiated at the persistent slip bands near or at the surfaces rather than process-induced volumetric defects in all cases. The fatigue behavior of L-PBF IN718 specimens was ~~corre~~lated with the sizes of grains and facets. Fatigue life estimation incorporating the NASGRO equation and $\sqrt{area}$ of the grain sizes was performed and shown to predict fatigue life within scatter bands of five.

Keywords: Laser powder bed fusion, Inconel 718, facet, NASGRO, fatigue life prediction.

Introduction

Laser powder bed fusion (L-PBF) is one of the most popular additive manufacturing (AM) technologies because it can fabricate intricate parts with higher accuracy [1,2]. Inconel 718 (IN718), a precipitation-strengthening Ni-base superalloy, is one of the most common materials for various AM technologies due to its excellent weldability [3]. Poor machinability of IN718 [4] also contributes to the adoption of the L-PBF method as an alternate option over conventional manufacturing methods. Interestingly, contrary to the typical laser powder bed fused (L-PBF) materials such as Ti-6Al-4V and 17-4 precipitation hardening stainless steel [5], the source of fatigue crack initiations in L-PBF IN718 is not always the process-induced volumetric defects in machined surface condition [6,7].

For L-PBF IN718, Wan et al. [8] reported that main fatigue cracks always initiated from the process-induced gas-entrapped pores (approximately spherical shaped with ~ 20 μm diameter) in the high cycle fatigue (HCF) regimes (~10^4 - 10^8 cycles [9,10]). Despite having similar sized defects, Yang et al. [11] observed that in HCF and very high cycle fatigue (VHCF, >10^8 cycles [12]) regimes, crack initiation can be either from volumetric defects or from crystallographic facets. An earlier study by Muhammad et al. [6] in HCF and VHCF regimes for two different test frequencies (5 Hz and 20 kHz) reported that the fatigue crack initiation exclusively occurred from crystallographic facets, even though the maximum defect diameter was ~ 40 μm [3]. These observations from the literature suggest competition between the defect- and facet-driven crack initiation mechanisms in the L-PBF IN718. Dodaran et al. [13] reported that for machined surface L-PBF IN718, defects do not cause initiation of fatigue cracks unless they are large enough to compete with the grain size. Hence, it is critical to understand

the factors governing this competition between the defects and facets to predict the fatigue behavior of L-PBF IN718 accurately.

Using the size of process-induced volumetric defects as the initial crack size is one of the most common analytical approaches to predict the fatigue life of AM parts [14–18] in machined surface condition. Use of the Murakami's $\sqrt{area}$ approach for calculating crack initiation size was also found to be effective in estimating the fatigue strength of AM parts [17,18]. Several works have incorporated Murakami's $\sqrt{area}$ approach into the NASGRO crack growth equation to predict fatigue lives of AM parts [14–16]. However, this approach might not be suitable for L-PBF IN718 parts where crack initiates from persistent slip bands (PSBs) rather than defects.

This study attempts to predict the fatigue life of L-PBF IN718 specimens by considering the largest grain size as the initial crack size. For this purpose, uniaxial fatigue specimens were fabricated using two different process parameters, followed by a series of heat treatments to obtain different microstructures. Uniaxial strain-controlled fatigue tests were performed on the machined specimens to obtain the fatigue lives. The fatigue life was predicted using the NASGRO equation considering the largest grain size as an equivalent crack size. Finally, a comparison between predicted and experimental fatigue lives was shown to assess the applicability of this model for predicting the fatigue behavior of L-PBF IN718.

Experimental methods

Two sets of oversized IN718 specimens were fabricated using argon gas atomized IN718 powders in an argon-purged environment via the L-PBF process utilizing an EOS M290 AM system. Out of two sets, one set of specimens was fabricated using the manufacturer-recommended process parameters, as listed in **Table 1**, which will be addressed as optimal specimens in this study. Another set of specimens was fabricated by intentionally bringing the machine out of calibration to induce more volumetric defects, which will be addressed as non-optimal specimens in this study. Details of experimental methods can be found in [13].

Table 1. EOS M290 manufacturer-recommended process parameters for fabrication of L-PBF IN718.

Laser power	285 W
Scanning velocity	960 mm/s
Layer thickness	40 µm
Hatching distance	110 µm

As listed in **Table 2**, two different heat treatment procedures were applied to the optimal and non-optimal L-PBF IN718 specimens before machining. All the heat treatments were conducted in an electric furnace in an argon environment. All specimens were stress-relieved at 1065°C for 1.5 hours according to the ASTM F3055-14a standard before removing from the build plate [19]. Following stress-relieving, the non-optimal test specimens underwent the hot isostatic pressing (HIP) step, followed by solution treatment and double aging according to ASTM F3055-14a and AMS 5664 standards [20–22], as illustrated in **Table 2**. Optimal test specimens, after stress-relieving, went through solution treatment and double aging according to ASTM F3055-14a and AMS 5664 standards [20–22].

Table 2. Heat treatment schedules for the optimal and non-optimal L-PBF IN718 specimens in this study [13].

Desig.	Stress-relieving	Cooling	HIP	Solution treatment	Cooling	Aging: Step 1	Aging: Step 2	Cooling
Optimal	1065°C for 1.5 hr	Furnace cooled	-	1066°C for 1 hr	Air cooled	760°C for 10 hr	650°C for 10 hr	Air cooled
Non-optimal	1065°C for 1.5 hr	Furnace cooled	1163°C at 102 MPa for 3 hr	1066°C for 1 hr	Air cooled	760°C for 10 hr	650°C for 10 hr	Air cooled

After the heat treatment, fatigue specimens were machined to the final geometry and dimensions according to ASTM E606 standard (see **Figure 1**) [23]. A scanning electron microscope (SEM) was used to conduct electron back-scattered diffraction (EBSD) scans on the longitudinal planes (i.e., the plane parallel to the axial direction of the specimens) to study grain morphology (see inverse pole figure (IPF) maps in **Figure 2**). The non-optimal sample contained larger grains (~ 4.6 times) compared to the optimal one, which might be attributed to the differences in their heat treatment schedules. For defect characterization, both the X-ray computational tomography scanning and optical microscope were used on the coupons extracted from both optimal and non-optimal specimens in the previous study [13]. The largest pores found in the optimal and the non-optimal specimens were ~ 20 and ~ 10 µm, respectively, which were significantly smaller than their respective columnar grain sizes.

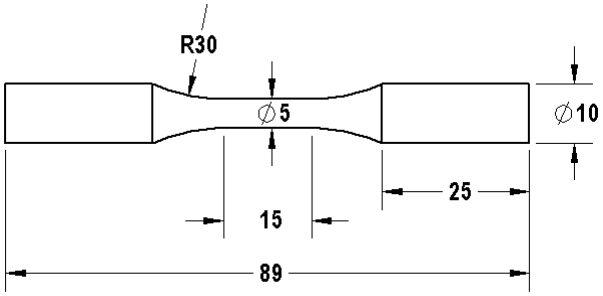

Figure 1. The final geometry of L-PBF IN718 uniaxial fatigue specimens (All the dimensions are in mm).

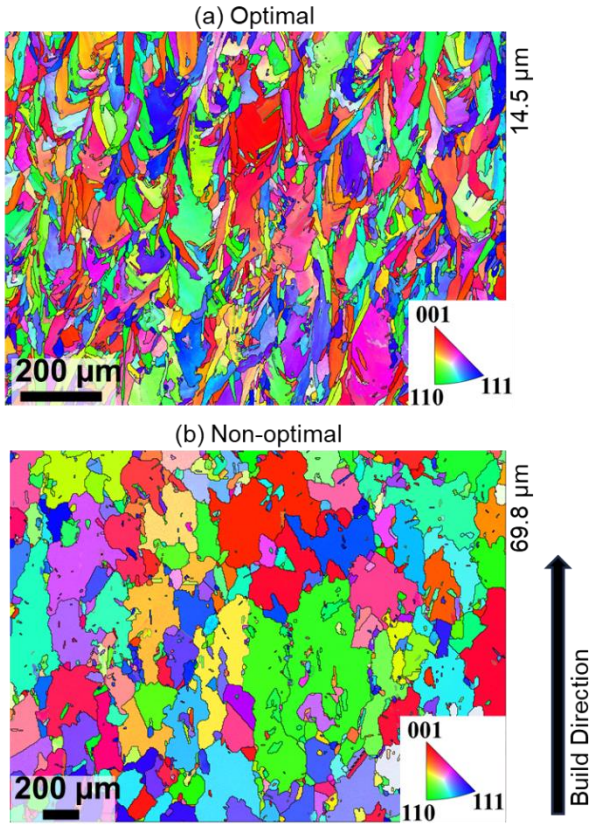

Figure 2. IPF maps of L-PBF IN718: (a) optimal and (b) non-optimal samples in the longitudinal planes.

Strain-controlled, uniaxial, fully-reversed fatigue tests ($R_\varepsilon = \varepsilon_{min}/\varepsilon_{max} = -1$) on optimal and non-optimal L-PBF IN718 specimens were conducted utilizing an MTS servo-hydraulic machine according to the ASTM E606 standard [23]. Different strain amplitudes ranging from 0.0020 mm/mm to 0.0060 mm/mm were applied, and at

least two specimens were tested for each strain amplitude. Fatigue tests were continued until the failure or pre-defined runout condition (10^7 reversals) was reached. Fractography was performed using SEM on selected fracture surfaces to identify the crack initiation mechanisms.

Fatigue life prediction method using NASGRO equation

Predictions of fatigue lives were made by integrating the NASGRO fatigue crack growth equation based on the size of fatigue critical defects measured via SEM [24]. Based on the fracture mechanics approach, the maximum stress intensity factor experienced in a material for an existing crack can be calculated as:

$$K_{max} = Y\sigma_{max}\sqrt{\pi a_i} \quad (1)$$

where K_{max} is the maximum stress intensity factor, σ_{max} is the maximum applied stress, Y is the shape factor, and a_i is the initial crack size.

A popular model for estimating the stress intensity factor and the fatigue limit is Murakami's $\sqrt{area}$ model [24]. It is a location-sensitive model where the square root of the projected area of a crack-initiating defect on the loading plane was considered the crack size. According to Murakami's $\sqrt{area}$ model [24], for defects located at the surface, the stress intensity factor along its crack front can be calculated as:

$$K_{max} = 0.65\sigma_{max}\sqrt{\pi\sqrt{area}} \quad (2)$$

For internal defects, the stress intensity factor can be calculated as:

$$K_{max} = 0.5\sigma_{max}\sqrt{\pi\sqrt{area}} \quad (3)$$

For the prediction of fatigue life, Paris law [25] and its modifications are widely employed [14–16]. A popular model among them is the NASGRO equation [26], which is a general crack growth equation that considers the mean stress effect, crack growth threshold (ΔK_{th}), and fracture toughness (K_c). NASGRO equation can be used to calculate the fatigue life of components and is given by [26]:

$$\frac{da}{dN} = C\left[\left(\frac{1-f}{1-R}\right)\Delta K\right]^n \frac{\left(1-\frac{\Delta K_{th}}{\Delta K}\right)^p}{\left(1-\frac{K_{max}}{K_C}\right)^q} \quad (4)$$

where R is the stress ratio, C is the intercept constant for $R = 0$, f is the Newman crack closure function, ΔK is the stress intensity factor range, n is the slope of the crack growth curve on a log-log scale (Paris exponent), ΔK_{th} is the threshold stress intensity factor range, K_c is the plane strain fracture toughness of the material, K_{max} is the maximum stress intensity factor (Eqs. (2-3)), and p and q are the empirical coefficients of crack growth rate in the crack nucleation and final fracture zone respectively.

To calculate fatigue life, Eq. (4) can be expressed as [27]:

$$N = \int_{a_i}^{a_c} \frac{1}{C\left[\left(\frac{1-f}{1-R}\right)\Delta K\right]^n \left(1-\frac{\Delta K_{th}}{\left(\frac{1-f}{1-R}\right)\Delta K}\right)^p} \quad (5)$$

where a_i is the initial crack size, and a_c is the critical crack size when the final failure occurs, i.e., when K_{max} exceeds K_c.

Results and discussion

Strain-life fatigue plot of optimal and non-optimal IN718 specimens is shown in **Figure 3**, which is also reported in [13,28]. Arrows in **Figure 3** indicate tests that met the runout condition. It is evident from **Figure 3** that, at all strain amplitudes, the optimal specimen exhibited higher fatigue life than the non-optimal ones. The difference in the fatigue life between both sets changes with the strain amplitude, and the difference is more significant at lower strain amplitudes. For example, at the higher strain amplitude of 0.0050 mm/mm, where the crack growth period is dominant in total fatigue life, the difference in fatigue lives between optimal and non-optimal specimens was only a factor of 2 ~ 3. On the other hand, at the lower strain amplitude of 0.0030 mm/mm, where crack initiation was the dominant mechanism, at least one order of magnitude longer fatigue lives were observed for optimal specimens. Even when all the optimal specimens reached runout conditions (at a strain amplitude of 0.0027 mm/mm), the non-optimal specimens failed below 10^6 cycles.

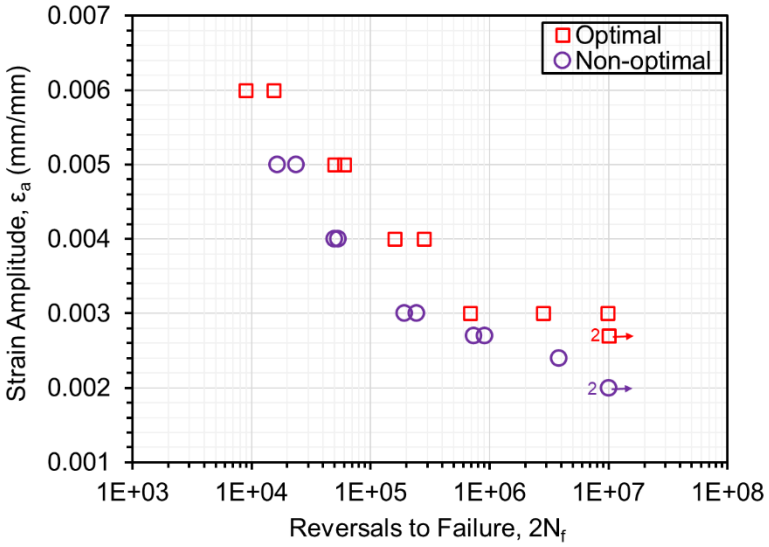

Figure 3. Strain-life fatigue plot of optimal and non-optimal L-PBF IN718 uniaxial specimens [13].

Fractography was conducted on selected optimal and non-optimal L-PBF IN718 specimens, some of which are presented in **Figure 4**. The presence of crystallographic facets at the crack initiation sites on all the fracture surfaces indicates the crack initiation from PSBs. Overall, larger facets were observed on the fracture surfaces of the non-optimal specimens compared to those of the optimal ones (see **Figure 4**). The size of the $\sqrt{area}$ of facets for specimens that failed at different strain amplitudes was measured, and each measurement was repeated at least three times. Irrespective of the loading amplitudes, the average facet sizes appeared to be similar within a specimen set. The average $\sqrt{area}$ of the facets for optimal specimens (i.e., fine grains) was ~ 94 µm, and for non-optimal specimens (i.e., coarse grains) was ~ 244 µm — a difference of a factor of more than 2. These facet sizes were comparable to the sizes of the largest grains in the two specimen sets (see IPF maps in **Figure 2**).

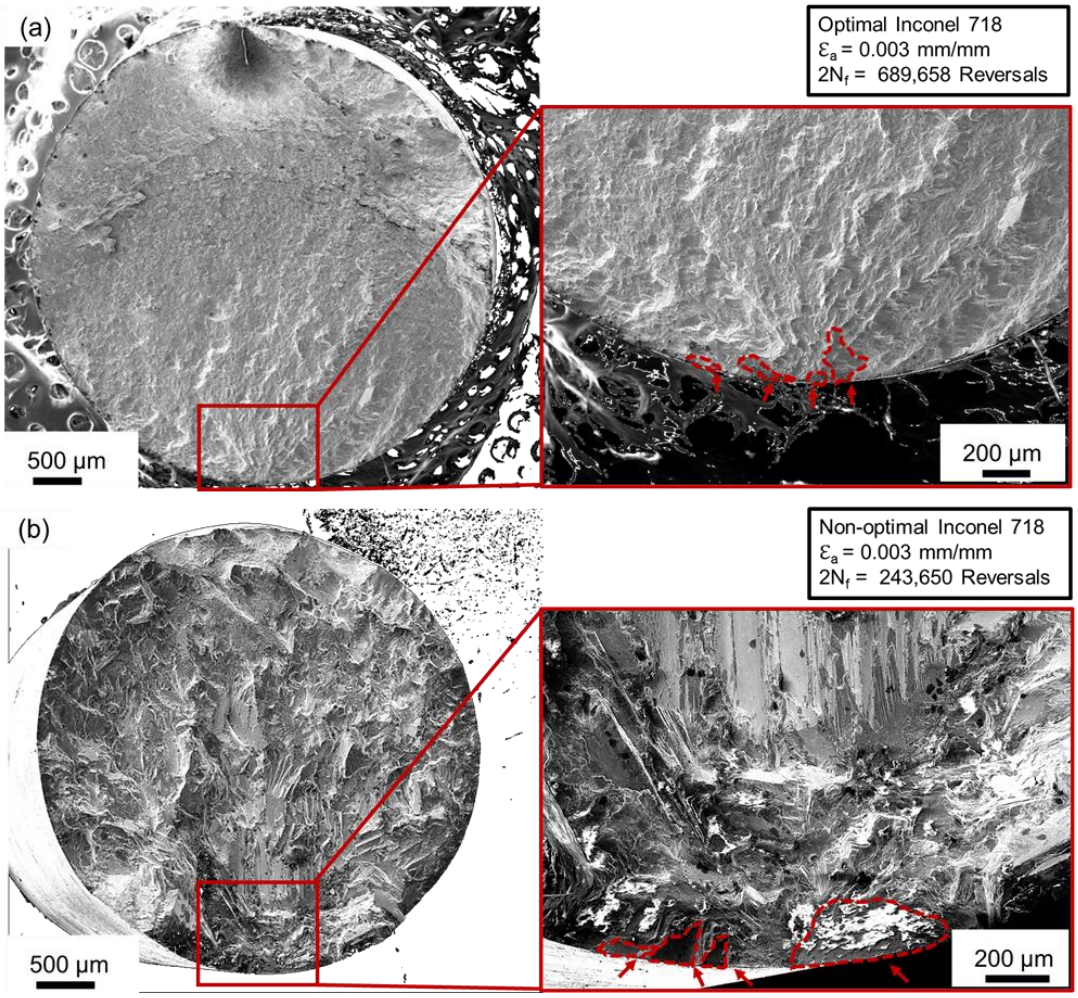

Figure 4. Fracture surfaces (a) optimal and (b) non-optimal L-PBF IN718 specimens.

Figure 6 presents the predicted fatigue life using the NASGRO equation (Eq. (5)) and the experimental fatigue life of optimal and non-optimal L-PBF IN718 specimens. Irrespective of the specimen sets and strain rate, cracks initiate from the surfaces for all specimens (**Figure 4**), and hence for the estimation of K_{max}, Eq. (2) was used. In **Figure 6**, the black line demonstrates the perfect prediction line, and the orange dashed, and blue dash-dotted lines demonstrate the scatter bands of the factor of 3 and 5, respectively. The fatigue life was calculated using the NASGRO equation (Eq. (5)), utilizing the $\sqrt{area}$ of the largest grain (measured from IPF maps obtained from EBSD scanning at the longitudinal planes) as the size of the defects. The assumption of the $\sqrt{area}$ of the largest grain as defect size was made based on the fact that the size of the facets, i.e., crack initiation sites, were comparable to the size of the columnar grains. Therefore, considering $\sqrt{area}$ of the largest columnar grain as defect size was a conservative approach. The values of constants and coefficients of the NASGRO equation were obtained by curve fitting on the experimental fatigue crack growth curve (generated by NASA Marshall Space Flight Center [29]) of L-PBF IN718 employing NASGRO fracture mechanics and fatigue crack growth software. The runout fatigue data were not included in the fatigue life estimation here. The $\sqrt{area}$ of the largest grain for optimal and non-optimal specimens in the longitudinal plane were ~ 127.26 and ~ 622.75 µm, respectively.

Figure 6 shows that fatigue life prediction of all non-optimal and 77.77% of the optimal specimens fall within the scatter band of 5. Note that there was a significant scatter (~ 1 order of magnitude) on the experimental fatigue data of the optimal specimens tested at 0.0030 mm/mm strain amplitude (see **Figure 5)**, which also impacted the fatigue life estimation (i.e., the data points which fall outside of the scatter bands of 5). In addition, fatigue life prediction of 77.77% non-optimal and 66.66% of the optimal specimens fall within the scatter bands

of 3. Therefore, the assumption of using the $\sqrt{area}$ of the largest grain as defect (or crack) size could not provide a good prediction of fatigue lives for optimal L-PBF IN718 specimens within the scatter bands of 5.

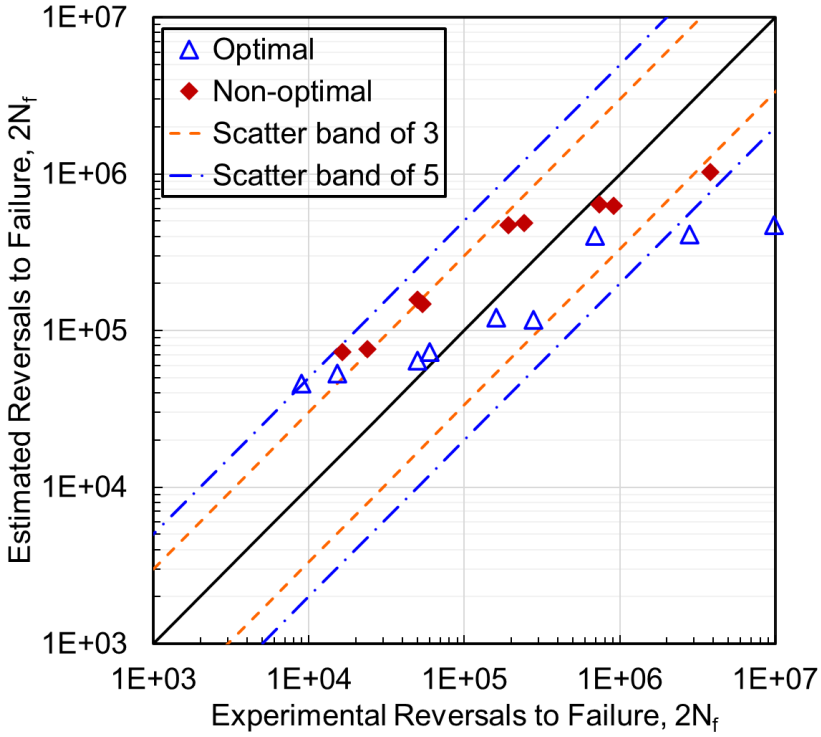

Figure 6. The predicted fatigue lives compared to the experimental data with the scatter bands of 3 and 5 for optimal and non-optimal L-PBF IN718.

Conclusions

This study investigated the uniaxial strain-controlled fatigue behavior of L-PBF IN718 specimens fabricated using optimal and non-optimal processing conditions. Fatigue behavior was correlated with microstructure and fracture surfaces. Furthermore, fatigue life modeling employing the NASGRO equation and $\sqrt{\text{area}}$ of the largest grain sizes of optimal and non-optimal specimens was performed. The findings of this study can be summarized as follows:

- Non-optimal L-PBF IN718 specimens consist of larger grains compared to the optimal ones, which can be attributed to the differences in the heat treatment conditions.
- Optimal L-PBF IN718 specimens exhibited superior fatigue performance compared to the non-optimal ones, which can be attributed to the smaller grain sizes compared to the non-optimal ones.
- Fatigue cracks for all L-PBF IN718 specimens initiated from PSBs instead of volumetric defects, irrespective of the processing conditions and heat treatment.
- Fatigue life prediction employing the NASGRO equation and $\sqrt{\text{area}}$ of the grain sizes for the non-optimal and majority of the optimal L-PBF IN718 specimens fall within the scatter bands of five. Therefore, using the $\sqrt{\text{area}}$ of the largest grain as the defect (or initial crack) size might not always provide a good prediction of fatigue life for L-PBF IN718.

Acknowledgment

This work was partially supported by the National Aeronautics and Space Administration (NASA) under Award No. 80MSFC18N0001.

References

[1] Gruber S, Grunert C, Riede M, López E, Marquardt A, Brueckner F, et al. Comparison of dimensional accuracy and tolerances of powder bed based and nozzle based additive manufacturing processes. J Laser Appl 2020;32:032016.

[2] Bremen S, Meiners W, Diatlov A. Selective Laser Melting. Laser Technik Journal 2012;9:33–8.

[3] Lingenfelter A. Welding of Inconel Alloy 718: A Historical Overview. Superalloys 718 Metallurgy and Applications (1989), TMS; 1989, p. 673–83.

[4] Choudhury IA, El-Baradie MA. Machinability of nickel-base super alloys: a general review. J Mater Process Technol 1998;77:278–84. https://doi.org/10.1016/S0924-0136(97)00429-9.

[5] Mostafaei A, Zhao C, He Y, Reza Ghiaasiaan S, Shi B, Shao S, et al. Defects and anomalies in powder bed fusion metal additive manufacturing. Curr Opin Solid State Mater Sci 2022;26:100974.

[6] Muhammad M, Frye P, Simsiriwong J, Shao S, Shamsaei N. An investigation into the effects of cyclic strain rate on the high cycle and very high cycle fatigue behaviors of wrought and additively manufactured Inconel 718. Int J Fatigue 2021;144:106038.

[7] Nezhadfar PD, Johnson AS, Shamsaei N. Fatigue behavior and microstructural evolution of additively manufactured Inconel 718 under cyclic loading at elevated temperature. Int J Fatigue 2020;136:105598.

[8] Wan H-Y, Zhou Z-J, Li C-P, Chen G-F, Zhang G-P. Enhancing Fatigue Strength of Selective Laser Melting-Fabricated Inconel 718 by Tailoring Heat Treatment Route. Adv Eng Mater 2018;20:1800307.

[9] Murakami Y, Miller KJ. What is fatigue damage? A view point from the observation of low cycle fatigue process. Int J Fatigue 2005;27:991–1005.

[10] Stephens RI, Fatemi A, Stephens RR, Fuchs HO. Metal Fatigue in Engineering, 2nd Edition. 2000.

[11] Yang K, Huang Q, Wang Q, Chen Q. Competing crack initiation behaviors of a laser additively manufactured nickel-based superalloy in high and very high cycle fatigue regimes. Int J Fatigue 2020;136:105580.

[12] Horst P, Adam TJ, Lewandrowski M, Begemann B, Nolte F. Very High Cycle Fatigue - Testing Methods. IOP Conf Ser Mater Sci Eng 2018;388:012004.

[13] Dodaran MS, Muhammad M, Shamsaei N, Shao S. Synergistic effect of microstructure and defects on the initiation of fatigue cracks in additively manufactured Inconel 718. Int J Fatigue 2022;162:107002.

[14] Romano S, Nezhadfar PD, Shamsaei N, Seifi M, Beretta S. High cycle fatigue behavior and life prediction for additively manufactured 17-4 PH stainless steel: Effect of sub-surface porosity and surface roughness. Theoretical and Applied Fracture Mechanics 2020;106:102477.

[15] Hamidi Nasab M, Romano S, Gastaldi D, Beretta S, Vedani M. Combined effect of surface anomalies and volumetric defects on fatigue assessment of AlSi7Mg fabricated via laser powder bed fusion. Addit Manuf 2020;34:100918.

[16] Muhammad M, Carrion PE, Shamsaei N. Fatigue life prediction of additive manufactured materials using a defect sensitive model. Proceedings of the 30th Annual International Solid Freeform Fabrication Symposium, 2019.

[17] Masuo H, Tanaka Y, Morokoshi S, Yagura H, Uchida T, Yamamoto Y, et al. Influence of defects, surface roughness and HIP on the fatigue strength of Ti-6Al-4V manufactured by additive manufacturing. Int J Fatigue 2018;117:163–79.

[18] Masuo H, Tanaka Y, Morokoshi S, Yagura H, Uchida T, Yamamoto Y, et al. Influence of defects, surface roughness and HIP on the fatigue strength of Ti-6Al-4V manufactured by additive manufacturing. Int J Fatigue 2018.

[19] ASTM International. ASTM F3055-14a Standard Specification for Additive Manufacturing Nickel Alloy (UNS N07718) with Powder Bed Fusion 2014.

[20] AMS5664: Nickel Alloy, Corrosion and Heat Resistant, Bars, Forgings, and Rings, 52.5Ni - 19Cr - 3.0Mo - 5.1Cb - 0.90Ti - 0.50Al - 18Fe, Consumable Electrode or Vacuum Induction Melted, 1950 °F (1066 °C) Solution Heat Treated, Precipitation Hardenable - SAE International

[21] NASA. MSFC-SPEC-3717-Specification for control and qualification of laser powder bed fusion metallurgical processes. 2017.

[22] International A. Standard Specification for Additive Manufacturing Nickel Alloy (UNS N07718) with Powder Bed Fusion F3055. ASTM Standard 2014:1–8.
[23] ASTM, ASTM E606/E606M. Standard Test Method for Strain-Controlled Fatigue Testing. ASTM Standards 2004.
[24] Murakami Y. Effects of Small Defects and Nonmetallic Inclusions on the Fatigue Strength of Metals. 2009.
[25] Paris P, Director A, Erdogan F. A Critical Analysis of Crack Propagation Laws. 1963.
[26] NASGRO® Fracture Mechanics & Fatigue Crack Growth Software |SwRI
[27] Zhang W, Wang Q, Li X, He J. A Simple Fatigue Life Prediction Algorithm Using the Modified NASGRO Equation. Math Probl Eng 2016;2016.
[28] Lee S, Shao S, Wells DN, Zetek M, Kepka M, Shamsaei N. Fatigue behavior and modeling of additively manufactured IN718: The effect of surface treatments and surface measurement techniques. J Mater Process Technol 2022;302:117475.
[29] Overview of Fatigue and Damage Tolerance Performance of Powder Bed Fusion Alloy N07718 Douglas Wells NASA MSFC Huntsville AL ASTM/NIST Workshop on Mechanical Behavior in Additive Manufactured parts 2016.